Nanoscale

PAPER

View Article Online
View Journal | View Issue

Cite this: *Nanoscale*, 2019, **11**, 22089

Elucidating ligand effects in thiolate-protected metal clusters using $Au_{24}Pt(TBBT)_{18}$ as a model cluster†

Sakiat Hossain, [a] Yukari Imai,[a] Daiki Suzuki,[a] Woojun Choi,[b] Zhaoheng Chen,[a] Taiyo Suzuki,[a] Mahiro Yoshioka,[a] Tokuhisa Kawawaki, [a,c] Dongil Lee *[b] and Yuichi Negishi *[a,c]

2-Phenylethanethiolate (PET) and 4-*tert*-butylbenzenethiolate (TBBT) are the most frequently used ligands in the study of thiolate (SR)-protected metal clusters. However, the effect of difference in the functional group between these ligands on the fundamental properties of the clusters has not been clarified. We synthesized $[Au_{24}Pt(TBBT)_{18}]^0$, which has the same number of metal atoms, number of ligands, and framework structure as $[Au_{24}Pt(PET)_{18}]^0$, by replacing ligands of $[Au_{24}Pt(PET)_{18}]^0$ with TBBT. It was found that this ligand exchange is reversible unlike the case of other metal-core clusters. A comparison of the geometrical/electronic structure and stability of the clusters between $[Au_{24}Pt(PET)_{18}]^0$ and $[Au_{24}Pt(TBBT)_{18}]^0$ revealed three things with regard to the effect of ligand change from PET to TBBT on $[Au_{24}Pt(SR)_{18}]^0$: (1) the induction of metal-core contraction and Au–S bond elongation, (2) no substantial effect on the HOMO–LUMO gap but a clear difference in optical absorption in the visible region, and (3) the decrease of stabilities against degradation in solution and under laser irradiation. By using these two clusters as model clusters, it is expected that the effects of the structural difference of ligand functional-groups on the physical properties and functions of clusters, such as catalytic ability and photoluminescence, would be clarified.

Received 18th August 2019,
Accepted 16th October 2019

DOI: 10.1039/c9nr07117b

rsc.li/nanoscale

Introduction

When a metal is reduced to fine particles of ~1 nm in diameter, the particles exhibit physical and chemical properties and functions that are different from ordinary metals. These physical and chemical properties and functions change significantly depending on the number of constituent atoms. Metal clusters with these characteristics are expected to be applied in diverse fields, such as energy, environment, and medical care.

To control the physical and chemical properties of such metal clusters, synthesis with atomic precision is essential. Thiolates (SRs),[1–19] selenolates,[20,21] alkynylates groups,[22] phosphines,[23,24] and carbon monoxide[25,26] can be used as ligands, and then metal clusters can be synthesized with atomic precision. Among them, thiolate-protected gold clusters ($Au_n(SR)_m$) have a high stability in the solution and solid state, and exhibit multiple physical/chemical properties and functions that are suitable for application including photoluminescence, redox behavior, and catalysis.[27] For these reasons, $Au_n(SR)_m$ clusters have been the subject of increasing research in recent years.[5]

In the study of $Au_n(SR)_m$ clusters, when 2-phenylethanethiolate (PET; Scheme S1(a)†) or 4-*tert*-butylbenzenethiolate (TBBT; Scheme S1(b)†) is used as a ligand, the single crystallization of clusters is relatively easy and the determination of the geometrical structure of $Au_n(SR)_m$ clusters is possible by single-crystal X-ray diffraction analysis (SCXRD).[28,29] Therefore, to understand the correlation between the chemical composition and geometrical structure and that between geometrical structure and physical properties, PET and TBBT have been the two most commonly used ligands in the study of $Au_n(SR)_m$ clusters. Because these SRs have substantially different functional groups (Scheme S1†), the resulting $Au_n(SR)_m$ clusters have different chemical compositions and geometrical structures.[28,29]

[a]*Department of Applied Chemistry, Faculty of Science, Tokyo University of Science, 1-3 Kagurazaka, Shinjuku-ku, Tokyo 162-8601, Japan.*
E-mail: negishi@rs.kagu.tus.ac.jp
[b]*Department of Chemistry, Yonsei University, Seoul 03722, Korea.*
E-mail: dongil@yonsei.ac.kr
[c]*Photocatalysis International Research Center, Tokyo University of Science, 2641 Yamazaki, Noda, Chiba 278-8510, Japan*

† Electronic supplementary information (ESI) available: Bond lengths, peak positions in SWV curves, additional schemes, characterization of a precursor, photograph of TLC and crystal, ESI mass and XPS spectra, HPLC chromatogram, crystal data of the product. CCDC 1944945. For ESI and crystallographic data in CIF or other electronic format see DOI: 10.1039/c9nr07117b

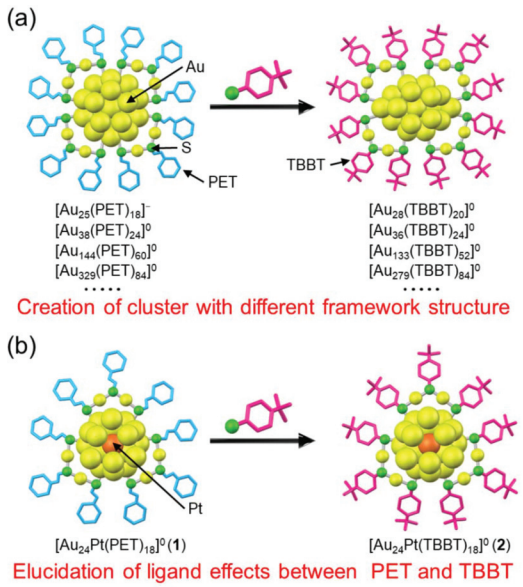

Fig. 1 Comparison between (a) previous work and (b) this work.

For example, when PET is used as the ligand, $Au_n(PET)_m$ clusters, such as $[Au_{25}(PET)_{18}]^-$, $[Au_{38}(PET)_{24}]^0$, $[Au_{52}(PET)_{32}]^0$, $[Au_{144}(PET)_{60}]^0$, and $[Au_{329}(PET)_{84}]^0$, are formed, whereas, in the case of TBBT, $Au_n(TBBT)_m$ clusters, such as $[Au_{28}(TBBT)_{20}]^0$, $[Au_{36}(TBBT)_{24}]^0$, $[Au_{52}(TBBT)_{32}]^0$, $[Au_{133}(TBBT)_{52}]^0$, and $[Au_{279}(TBBT)_{84}]^0$, are generated. The numbers of gold atoms and ligands are the same in $[Au_{52}(PET)_{32}]^0$ and $[Au_{52}(TBBT)_{32}]^0$, but their framework structures are significantly different.[30,31] $Au_n(SR)_m$ clusters with various chemical compositions and geometrical structures have been synthesized by using a number of such ligands that are suitable for single crystallization (Fig. 1(a)).

In addition to the chemical composition of the cluster, the stability, electronic structure, and functions of $Au_n(SR)_m$ clusters change depending on the functional-group structure of the ligand.[9,28–42] For example, it has been demonstrated that properties of $Au_{25}(SR)_{18}$, such as the stability in solution, reducibility, dissociation pattern under laser irradiation, quantum yield of photoluminescence, and catalytic activity, along with other properties, differ depending on the functional-group structure of the ligand. Therefore, the selection of the ligand functional group is essential in the functionalization of $Au_n(SR)_m$ clusters. Although PET and TBBT are the most frequently used ligands when studying $Au_n(SR)_m$ clusters, the effects of the ligand type (difference in functional group) on the electronic structure, stability, and function of $Au_n(SR)_m$ clusters are not well-known. To obtain detailed information regarding the effects of these different uses, it is essential to synthesize $Au_n(SR)_m$ clusters with the same number of metal atoms, number of ligands, and framework structure using PET and TBBT. However, no reports exist on the synthesis of the pair of $Au_n(SR)_m$ clusters described above.

The difference in bulkiness of the functional groups of the two ligands is closely related to this reason. In general, the $Au_n(TBBT)_m$ clusters are synthesized by replacing the PET ligand of the $Au_n(PET)_m$ clusters with TBBT *via* a ligand-exchange reaction.[43–46] Because TBBT has a bulky phenyl group next to S, unlike PET (Scheme S1†), an increase in the number of exchanged ligands in this reaction causes repulsion between the phenyl groups at the cluster surface, which result in stress induction on the framework structure of the cluster. As a result, ligand exchange from PET to TBBT causes changes in the chemical composition and framework structure of the cluster (Fig. 1(a)).[43] Thus, it can be presumed that to synthesize the pair of $Au_n(SR)_m$ clusters using PET and TBBT, it is necessary to use a cluster with a strong metal framework that can withstand the stress induced by repulsion between the ligands, as a precursor. Previous studies have shown that when the central atom of $Au_{25}(SR)_{18}$ (SR = PET or 1-dodecanethioate) is replaced with palladium (Pd) or platinum (Pt) ($[Au_{24}M(SR)_{18}]^0$; M = Pd or Pt), the framework structure of the cluster becomes stronger.[47,48] Furthermore, recent studies have revealed that this type of central-atom substitution can create an electrochemical catalyst with a high hydrogen-generation ability.[8,49]

The purpose of this study was to: (1) synthesize metal clusters with the same number of metal atoms, number of ligands, and framework structure using PET and TBBT; and (2) elucidate the effect of the difference in functional groups between PET and TBBT on the cluster through a direct comparison of the geometrical/electronic structure and stability between the obtained pair of clusters (Fig. 1(b)). To this end, we exchanged the ligand of $[Au_{24}Pt(PET)_{18}]^0$ from PET to TBBT. Consequently, we synthesized $[Au_{24}Pt(TBBT)_{18}]^0$ with the same number of metal atoms, number of ligands, and framework structures as $[Au_{24}Pt(PET)_{18}]^0$. We found that this ligand exchange is reversible unlike the case of other metal-core clusters. For the two $[Au_{24}Pt(SR)_{18}]^0$ (SR = PET or TBBT) obtained in this way, we studied their geometrical/electronic structure and stability. We could clarify details on the effect of differences between the two functional groups on the geometrical structure, optical absorption, electrochemical properties, stability in solution, and that against laser irradiation.

Results and discussion

Synthesis of $[Au_{24}Pt(TBBT)_{18}]^0$

The objective cluster was synthesized by stirring $[Au_{24}Pt(PET)_{18}]^0$ (cluster **1**) (Fig. S1 and Scheme S2(a)†) and 4-*tert*-butylbenzenethiol in toluene to exchange the ligand of the cluster from PET to TBBT. After the reaction was completed, excess thiol and by-products were removed from the product by washing with methanol, and the product purity was further improved by thin-layer chromatography (TLC; Fig. S2 and Scheme S2(b)†).

Fig. 2(a) shows the optical absorption spectrum of the obtained product (cluster **2**). In the absorption spectrum,

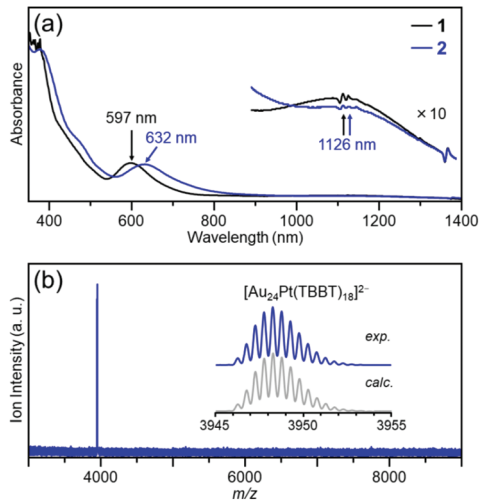

Fig. 2 Characterization of the product (cluster **2**); (a) optical absorption spectrum and (b) negative-ion ESI mass spectrum. In (a), optical absorption spectrum of cluster **1** is also shown for comparison purpose. In (b), cluster **2** was ionized to di-anion $[Au_{24}Pt(TBBT)_{18}]^{2-}$ during electrospraying. This ionization of the cluster is often observed in the literature.[49]

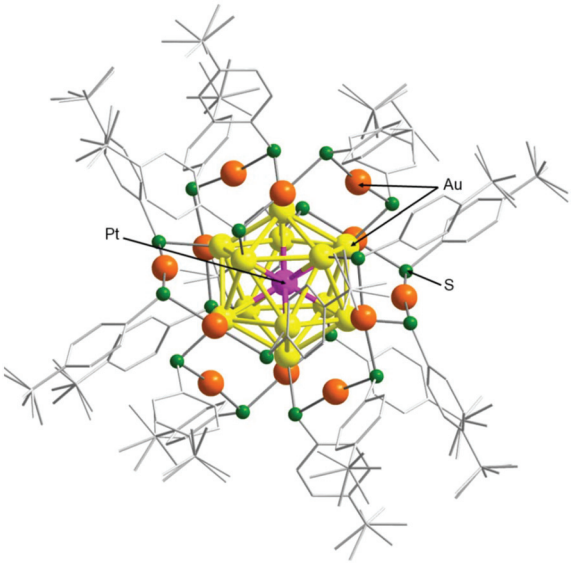

Fig. 3 Geometrical structure determined by SCXRD for cluster **2**. In the crystal, the counter anion was not observed, which is consistent with the interpretation that the product was neutral $[Au_{24}Pt(TBBT)_{18}]^0$.

peaks appear at approximately 1125 and 630 nm. Overall, the characteristics of this absorption spectrum are similar to those of cluster **1**.[48] Fig. 2(b) shows the negative-ion electrospray ionization (ESI) mass spectrum of cluster **2**. In the mass spectrum, a peak that is attributed to $[Au_{24}Pt(TBBT)_{18}]^{2-}$ appeared at m/z = 3948.2 (inset of Fig. 2(b)). In the positive-ion ESI mass spectrum of cluster **2**, which included Cs^+ in the solution, a peak that is attributed to $[Au_{24}Pt(TBBT)_{18}Cs_2]^{2+}$ appeared at m/z = 4081.2 as a main peak (Fig. S3†). In the X-ray photoelectron spectrum of cluster **2**, a weak-intensity peak that is attributed to Pt $4f_{7/2}$ and $4f_{5/2}$ was observed at around 75.4 and 79.2 eV, respectively (Fig. S4†). In the reversed-phase high-performance liquid chromatogram (HPLC), a single sharp peak was observed at the retention time that is expected for the neutral cluster (Fig. S5†). These results show that a neutral $[Au_{24}Pt(TBBT)_{18}]^0$ with the same number of metal atoms, number of ligands, and charge state as cluster **1** was synthesized.

To confirm that cluster **2** has a framework structure which is similar to that of cluster **1**, we determined the geometrical structure of cluster **2** *via* SCXRD. We used a slow evaporation method for crystallization and obtained dark-green single crystals (Fig. S6†). Fig. 3 shows the overall structure of cluster **2** that was determined by SCXRD. Cluster **2** has a geometrical structure in which six $Au_2(TBBT)_3$ staples surround an icosahedral $Au_{12}Pt$ core. This geometry is similar to that of cluster **1**.[50]

Unfortunately, it is challenging to determine the position of Pt using only SCXRD in this geometrical structure. Pt belongs to the same period as Au in the periodic table, and both elements have similar electron numbers (Pt; 78, Au; 79). Because the elements are discriminated by electron density in SCXRD, it is difficult to distinguish Pt from Au, which have very similar electron densities. However, for $[Au_{24}Pt(SR)_{18}]^0$, density functional theory (DFT) calculations predicted that the geometrical structure in which Pt is located at the center of the metal core is thermodynamically most stable.[51] The optical absorption spectrum of cluster **1** is similar to the theoretical absorption spectrum that is predicted for $[Au_{24}Pt(SR)_{18}]^0$ with the geometry described above.[48] The optical absorption spectrum of cluster **2** is similar to that of cluster **1** (Fig. 2(a)). These results indicate that Pt is located at the center of the metal core in cluster **2** (Fig. 3).

We found that cluster **2** can be returned to cluster **1** by a reaction between cluster **2** and 2-phenylethanethiol (Fig. 4). PET and TBBT have different functional-group structures and charge states[52] of S. However, this result demonstrates that when both clusters have a similar framework structure, the ligand exchange from TBBT to PET is also possible similar to that from PET to TBBT.

In this way, we succeeded in exchanging the PET ligand with TBBT while maintaining the number of metal atoms, the number of ligands, and the framework structure of cluster **1**. As described above, in the reaction between an $Au_n(PET)_m$ cluster and 4-*tert*-butylbenzenethiol, changes commonly occur in the number of metal atoms, number of ligands, and/or framework structure of the cluster with the number of exchanged ligands (Fig. 1(a)).[28,29,43–46] In this work, we have succeeded in preventing the deformation of the framework structure by using cluster **1**, which has a strong metal framework, as a precursor cluster.

Several examples exist in the syntheses of a pair of $Au_n(SR)_m$ clusters using PET and TBBT, such as $[Au_{20}(SR)_{16}]^0$ and $[Au_{52}(SR)_{32}]^0$.[30,31,53,54] However, for $[Au_{20}(SR)_{16}]^0$, the geometrical structure of $[Au_{20}(PET)_{16}]^0$ has not yet been clarified experimentally.[55] Regarding $[Au_{52}(SR)_{32}]^0$, as described above, the framework structures of $[Au_{52}(PET)_{32}]^0$ and $[Au_{52}(TBBT)_{32}]^0$ are

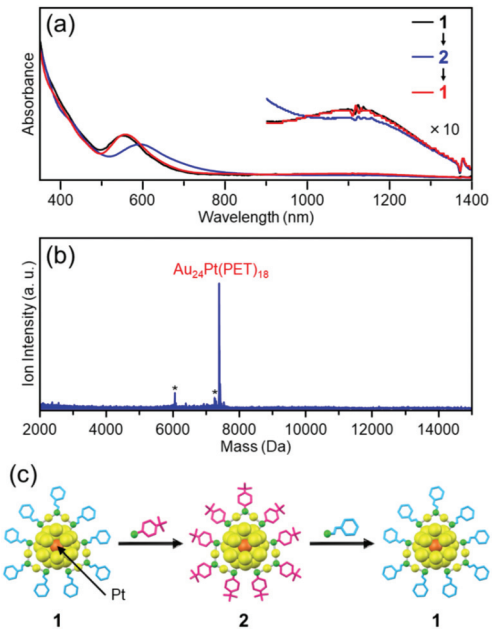

Fig. 4 Reaction of cluster **2** with 2-phenylethanethiol. (a) Optical absorption spectrum of the product with those of cluster **1** and starting cluster **2**. (b) Negative-ion MALDI mass spectrum of the product. (c) Schematic of the reversibility of the reaction. In (b), the asterisks indicate laser-fragments (see Fig. 9).

different.[30,31] In contrast, cluster **2** has the same framework structure as cluster **1**. By using these two clusters, it is possible to elucidate the effect of the difference in the functional group between PET and TBBT on the structure, stability, and physical and chemical properties of the clusters.

Ligand effects

By using clusters **1** and **2**, the effects of the difference in functional group between PET and TBBT on the geometric structure, electronic structure, and stability of $Au_n(SR)_m$ clusters were investigated.

Geometrical structure. As mentioned above, clusters **1** and **2** have similar framework structures (Fig. 3). Nonetheless, a closer inspection of the bond length revealed differences between the geometrical structures of the two clusters.

Fig. 5(a) compares the Pt–Au_{surf} (Au_{surf} is Au of the metal core surface) bond lengths between clusters **1** and **2**.[50] As described below, in both cases, the geometrical structure is distorted owing to the Jahn–Teller effect.[56] Because of the resulting strain, for cluster **1**, twelve bond lengths are distributed continuously in a bond-length range of 2.76–2.80 Å. However, in cluster **2**, the twelve bonds are divided into two types of bond lengths, six are approximately 2.76 Å and the remaining six are approximately 2.79 Å. Similar differences in distributions of bond lengths were observed in the bond-length distribution of the Au_{surf}–Au_{surf} (Fig. 5(b)), the Au_{surf}–S_{surf} (Fig. 5(c); S_{surf} is S bonded to Au_{surf}), the S–C (Fig. 5(d), Au_{surf}–Au_{staple} (Fig. S7(a) and Table S1;† Au_{staple} is Au in staple), and Au_{staple}–S (Fig. S7(b) and Table S1†) bonds. These

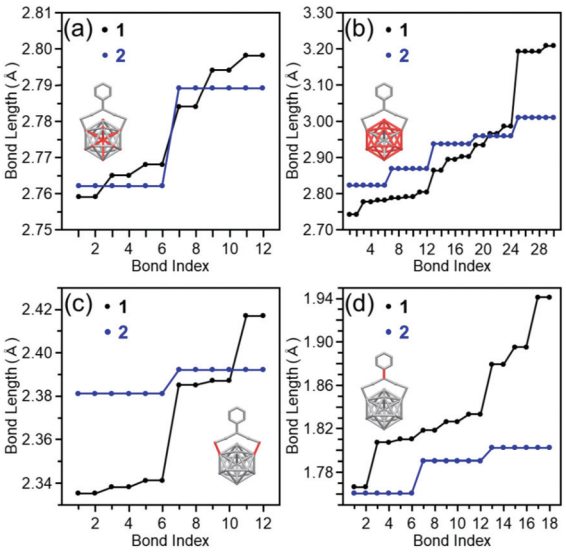

Fig. 5 Comparison of bond lengths between clusters **1** and **2**; (a) Pt–Au_{surf}, (b) Au_{surf}–Au_{surf}, (c) Au_{surf}–S_{surf}, and (d) S–C bonds. The bond lengths of cluster **1** were extracted from ref. 50.

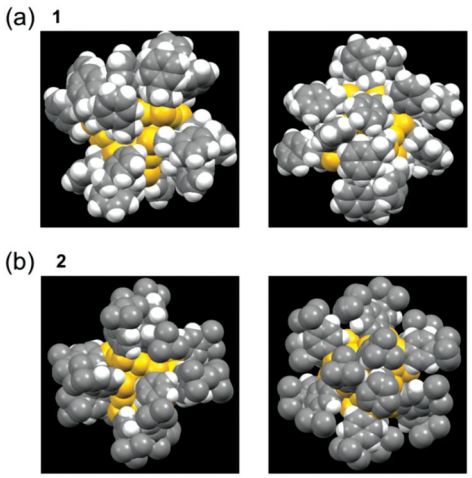

Fig. 6 Space-filling models obtained from SCXRD for clusters (a) **1** and (b) **2**. The space-filling models of cluster **1** were reproduced from ref. 50. In (a) and (b), two patterns from different angles are shown for each cluster. Copyright 2016 Royal Society of Chemistry.

results show that, although clusters **1** and **2** have broadly similar framework structures, differences exist in the distortion of their structures. According to the space-filling model, the phenyl groups are strongly gathered three by three at the cluster surface in cluster **2** (Fig. 6). It can be considered that cluster **2** has a geometrical structure with a high symmetry compared with cluster **1** because of this interaction between phenyl groups.

Considering the average bond length (Table 1), the Pt–Au_{surf} and Au_{surf}–Au_{surf} bonds are shorter and the Au_{surf}–S_{surf} bond is longer in cluster **2** than in cluster **1**. Therefore, cluster **2** has a compact metal core and $Au_2(SR)_3$ staples away from the

Table 1 Comparison of bond lengths between clusters **1** and **2**

Bond type	Cluster 1	Cluster 2
Pt–Au_{surf}	2.778 ± 0.015[a]	2.776 ± 0.014[a]
Au_{surf}–Au_{surf}	2.921 ± 0.155[a]	2.919 ± 0.067[a]
Au_{surf}–S_{surf}	2.367 ± 0.031[a]	2.387 ± 0.006[a]
S–C	1.842 ± 0.050[a]	1.784 ± 0.018[a]

[a] These values were extracted from ref. 50.

metal core surface compared with the cluster **1**. Based on the pK_a values of the aromatic ligand (pK_a = ~10 in DMSO), 4-*tert*-butylbenzenethiol, and the aliphatic ligand (pK_a = ~17 in DMSO), 2-phenylethanethiol,[52] TBBT is assumed to possess S with a lesser electron-donating property compared with PET. Because of this difference in pK_a, in cluster **2**, the Au–S bond is thought to be weaker than in cluster **1** and the $Au_2(SR)_3$ staple is distant from the metal core.[29]

Electronic structure. The following has come to light from previous studies for $Au_{24}Pt(SR)_{18}$ (SR = PET or 1-hexanethiolate (C6)): (i) as for $Au_{24}Pt(SR)_{18}$, the total number of valence electrons of the cluster satisfies the closed-shell electron structure as a divalent negative ion ($[Au_{24}Pt(SR)_{18}]^{2-}$), and in this $[Au_{24}Pt(SR)_{18}]^{2-}$, the energy of the highest occupied molecular orbital (HOMO) is triply degenerated (left side in Fig. 7(a)); (ii) for $[Au_{24}Pt(SR)_{18}]^0$, which has been isolated frequently in experiments, the total number of valence electrons is two less than the number of closed-shell electrons, which leads to the Jahn–Teller effect. As a result, in $[Au_{24}Pt(SR)_{18}]^0$, the triple degeneracy of the HOMO is resolved, which leads to the appearance of new HOMO and lowest unoccupied molecular orbital (LUMO) (right side in Fig. 7(a)); (iii) in $[Au_{24}Pt(SR)_{18}]^0$, the HOMO and LUMO are P-type orbitals, and transition between the HOMO and LUMO is prohibited. Therefore, the HOMO–LUMO transition could not be observed by using optical absorption spectroscopy. In the optical absorption spectrum of $[Au_{24}Pt(SR)_{18}]^0$, the peak near 1125 nm (1.10 eV) represents the transition from HOMO−1 to LUMO (α; right side in Fig. 7(a)), and the peak at around 600 nm (2.08 eV) is attributed to the transition from HOMO to LUMO+1 (β; right side in Fig. 7(a)).[56]

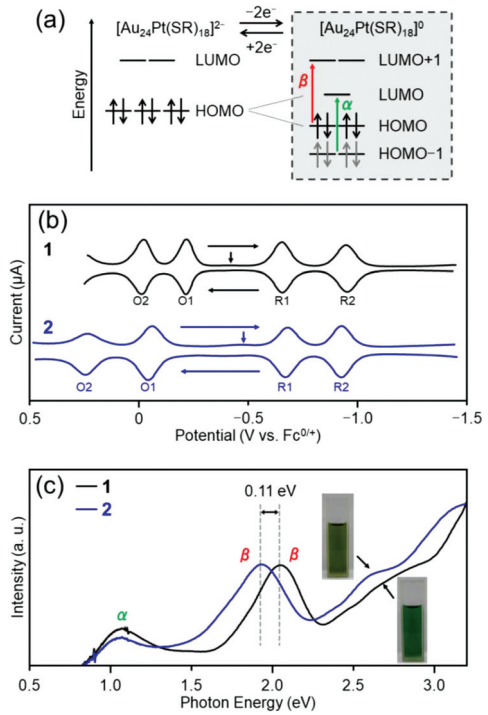

Fig. 7 Electronic structures of clusters **1** and **2**; (a) orbitals predicted by DFT calculation for $Au_{24}Pt(SR)_{18}$, (b) SWV curves and (c) optical absorption spectra. The schematic in (a) is adapted from ref. 56. In (c), the vertical arrows indicate the solution open-circuit potential. Copyright 2015 American Chemical Society.

In this study, to examine the effect of the difference in ligands on the electronic structure of $[Au_{24}Pt(SR)_{18}]^0$, square-wave voltammetry (SWV) was performed for both clusters. The SWV curves of clusters **1** and **2** are shown in Fig. 7(b). The shapes of the curves of the two clusters are similar to those of $[Au_{24}Pt(C6)_{18}]^0$,[56] which indicates that the Jahn–Teller effect is present in clusters **1** and **2** like in $[Au_{24}Pt(C6)_{18}]^0$. For both clusters, the HOMO–LUMO gap (right side in Fig. 7(b)) was estimated by subtracting the charging energy ($E_{O1} - E_{O2}$) from the electrochemical energy gap ($E_{R1} - E_{O1}$; here, E_{R1} indicates the peak potential of R1) (Table S2†).[56] Both were found to have a HOMO–LUMO gap of a similar magnitude (0.30 eV for cluster **1** and 0.33 eV for cluster **2**). Therefore, the difference in distortion of the framework structure has a minimal influence on the extent of degenerate resolution. Conversely, a large difference was found in $E_{O1} - E_{O2}$, which indicates that there is a significant difference in the charging energy[57] between clusters **1** and **2**.

Based on the optical absorption spectra (Fig. 2(a)), we also considered the effect of difference between the two functional groups on the α and β transition (right side in Fig. 7(a)). Fig. 7(c) shows the optical absorption spectra of the trichloroethylene solutions of clusters **1** and **2**, with the horizontal axis represented in terms of energy (eV). The first peak α appears near 1125 nm (1.10 eV) in both absorption spectra. As mentioned previously, this peak can be attributed to the transition from HOMO−1 to LUMO. Because the d orbital of Pt is largely involved in HOMO−1,[56] the energy of HOMO−1 changes considerably if the substitution position of Pt is different.[51] However, Pt is located at the center of the metal core in clusters **1** and **2**. Therefore, there is a minimal difference in the positions of this orbital between the two clusters, which results in no substantial change in the position of peak α in the spectrum between the two clusters. On the other hand, there is a difference in the position of peak β near 600 nm (1.95 eV) between the two clusters; in cluster **2**, the peak shifts to a low-energy region by approximately 35 nm (0.11 eV) compared with cluster **1**. Owing to this difference in peak position in the visible-light region, the colors of the cluster solution are slightly different (Fig. 7(c)). For LUMO+1, the orbital that is derived from S is also involved, in addition to the orbital of the metal core.[58] Because aliphatic hydrocarbon and aromatic

hydrocarbon are present next to S in PET and TBBT, respectively, the charge state of S should differ between PET and TBBT (see pK_a values described in the previous section). The difference in the charge state of S is considered to be the cause of the difference in the energy level between HOMO and LUMO+1 for the two clusters.

Stabilities. The effects of the ligand differences on the stabilities against degradation in a solution and under laser irradiation were investigated.

For the resistance against degradation in a solution, the clusters were dissolved in a solvent and the change was examined by using optical absorption spectroscopy. The time dependence of the change in the optical absorption spectrum of the toluene solution of cluster **1** and cluster **2** at 80 °C is shown in Fig. 8(a) and (b), respectively. Because the optical absorption of toluene appears at a wavelength longer than 1100 nm, peak α (Fig. 7(a) and (c)) could not be observed in this experiment. For cluster **1**, there was no substantial change in the optical absorption spectrum over the course of 5 h, as shown in Fig. 8(a). In contrast, the shape of the optical absorption spectrum for cluster **2** changed gradually with time (Fig. 8(b)). A similar phenomenon was observed for the toluene solution at 60 °C (Fig. S8†) and the tetrahydrofuran (THF) solution at 60 °C (Fig. S9†). These results indicate that ligand exchange from PET to TBBT reduces the $[Au_{24}Pt(SR)_{18}]^0$ stability in a solution.

Previous studies on $Au_{25}(PET)_{18}$ revealed that when $Au_{25}(PET)_{18}$ is allowed to stand in solution, the clusters undergo oxidation and induce a peeling-off reaction of the Au(I)-PET complex.[40] Because $[Au_{24}Pt(SR)_{18}]^0$ has a geometrical and electronic structures similar to $Au_{25}(SR)_{18}$,[50,56] $[Au_{24}Pt(SR)_{18}]^0$ degradation in solution in this study is presumed to be caused by the same reaction. Based on the O1 peak position in the SWV curve (Fig. 7(b)), cluster **2** requires more energy for oxidation than cluster **1**, which means that cluster **2** has an electronic structure that is more difficult to oxidize than cluster **1**. In cluster **2**, although the ligands are strongly gathered three by three at the cluster surface, different from cluster **1**, it is unlikely that the proportion of metal surfaces that are exposed to oxygen attack is high (Fig. 6). However, in cluster **2**, the Au–S bond is extended compared with cluster **1** (Table 1). From these results, it can be considered that cluster **2** is more easily degraded in a solution than cluster **1** because in cluster **2** the Au–S bond is more prone to breakage than in cluster **1**.

For stability under laser irradiation, we compared the extent of dissociation of the two clusters in matrix-assisted laser desorption/ionization (MALDI) mass spectrum.[59] Fig. 9(a) and (b) show the negative-ion MALDI mass spectra of clusters **1** and **2** measured at identical laser intensities, respectively. In Fig. 9(a), peaks assigned to $Au_{24}Pt(PET)_{17}$ and $Au_{20}Pt(PET)_{14}$ were observed as main peaks, in addition to the peak attributed to the parent $Au_{24}Pt(PET)_{18}$. The peak of $Au_{24}Pt(PET)_{17}$ is assumed to be formed by PET detachment from $Au_{24}Pt(PET)_{18}$ and the peak of $Au_{20}Pt(PET)_{14}$ is assigned to $Au_4(PET)_4$ detachment from cluster **1** (Fig. S10(a)†). These dissociation peaks were observed in our previous study on cluster **1**.[60] Fig. 9(b) shows the MALDI mass spectrum of cluster **2**, which was measured at the same laser intensity. In the mass spectrum, no peak appears that could be attributable to the parent cluster (cluster **2**), which suggests that cluster **2** underwent dissociation at this laser intensity. These results demonstrate that cluster **2** is more unstable under laser irradiation than cluster **1**. Actually, to the best of our knowledge, there are no reports in which the parent TBBT-protected metal cluster was observed in the MALDI mass spectrum.[43]

As described above, in cluster **2**, the Au–S bond is extended compared with cluster **1**. Because the dissociation of both clusters involves SR detachment, the difference in this bonding strength is thought to be responsible for the difference in stability. However, the dissociation pattern differs in both clusters. For example, for cluster **2**, the main peaks are $Au_{23}Pt(TBBT)_{16}$, $Au_{22}Pt(TBBT)_{15}$, and $Au_{19}Pt(TBBT)_7$, which are

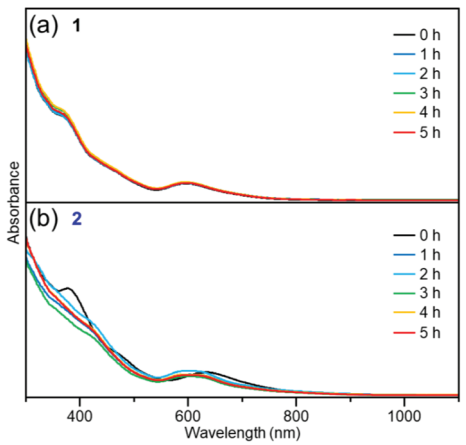

Fig. 8 Time dependences of absorption spectra of (a) cluster **1** in toluene (1×10^{-5} M) at 80 °C and (b) cluster **2** in toluene (1×10^{-5} M) at 80 °C.

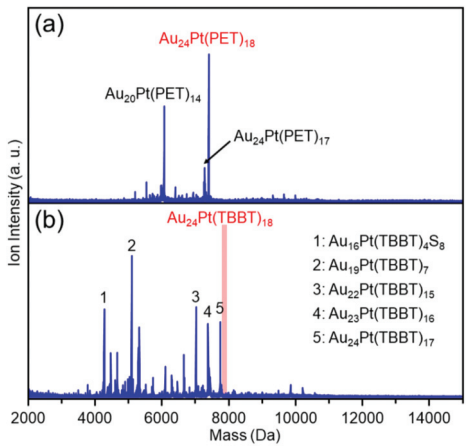

Fig. 9 Negative-ion MALDI mass spectra of clusters (a) **1** and (b) **2** recorded at same laser fluence. Only main fragment-peaks are assigned in these spectra. Details of laser-fragment patterns are described in Fig. S10.†

produced by the dissociation of $Au(TBBT)_2$, $Au_2(TBBT)_3$, or $Au_5(TBBT)_{11}$ from cluster **2**, respectively (Fig. S10(b)†). However, for cluster **1**, this type of dissociation pattern was not observed even at an increased laser intensity (Fig. S10(a)†). From these results, it is inferred that the difference in dissociation mechanism is also involved in the origin of the difference in stability against laser dissociation. Despite many uncertainties regarding the factors of the difference in stability remain, we expect that in the future more information would be obtained on the dissociation mechanism of the two clusters, which would improve the understanding of the difference in their ease of dissociation.

Comparison with previous studies. There are several reports on the ligand effects on the basic properties of the thiolate-protected metal clusters before our study. For example, Jin *et al.* have synthesized $[Au_{25}(SNAP)_{18}]^-$ (SNAP = 2-naphthalenethiolate) and reported the difference in geometrical/electronic structures, stabilities and catalytic activity between $[Au_{25}(PET)_{18}]^-$ and $[Au_{25}(SNAP)_{18}]^-$.[40] Also, Dass *et al.* have synthesized $[Au_{38}(SPh)_{24}]^0$ (SPh = benzenethiolate) and discussed the difference in geometrical/electronic structures, stabilities and fragmentation energies between $[Au_{38}(PET)_{24}]^0$ and $[Au_{38}(SPh)_{24}]^0$, although they could not obtain the geometrical structure of $[Au_{38}(SPh)_{24}]^0$ by SC-XRD in this study.[35] A part of our results is well consistent with their results, implying that the results obtained in our study (PET *vs.* TBBT) are predictable from the previous works using $Au_n(SR)_m$ clusters containing the ligands similar to TBBT. However, in this study, we demonstrated experimentally the expected effect of the ligand by a direct comparison between clusters **1** and **2**. We expect that the effects from the structural differences of the ligand functional-groups on the physical properties and functions of clusters, such as the catalytic ability[61] and photoluminescence,[62] would also be clarified in future by using these two clusters as model clusters.

Conclusions

In this study, we successfully synthesized $[Au_{24}Pt(TBBT)_{18}]^0$ with the same number of metal atoms, number of ligands, and framework structure as $[Au_{24}Pt(PET)_{18}]^0$, which has a strong metal core, by replacing the ligand from PET to TBBT. We found that this ligand exchange is reversible unlike the case of other metal-core clusters. By using the obtained pair of clusters, $[Au_{24}Pt(PET)_{18}]^0$ and $[Au_{24}Pt(TBBT)_{18}]^0$, we examined the effects of functional-group difference on the geometrical structure, electronic structure, and stability of the clusters. As a result, we found that the following three effects are induced when the ligand is changed from PET to TBBT in $[Au_{24}Pt(SR)_{18}]^0$:

(1) The metal core shrinks and the Au–S bond expands.

(2) There is no significant difference in HOMO–LUMO gap, but a clear difference is caused in the optical absorption in the visible region.

(3) The stability worsens in a solution and under laser irradiation.

By using these two clusters as model clusters, we expect that the effects of the structural difference of ligand functional-groups on the physical properties and functions of clusters, such as catalytic ability[61] and photoluminescence,[62] would be clarified.

However, it should be noted that the effect of the functional-group difference revealed in this study is that in $[Au_{24}Pt(SR)_{18}]^0$. If the framework structure of the cluster were changed, the magnitude of the stress generated by repulsion between the ligands and the resulting effect of the difference in the functional-group structure on the cluster would also differ. This study confirmed that when the metal core is strengthened, thiolate-protected metal clusters with the same number of metal atoms, number of ligands, and framework structure can be synthesized by using PET and TBBT. We expect that, based on this concept, other clusters with the same number of metal atoms, number of ligands, and framework structure would be synthesized by using PET and TBBT. If this is achieved, we could acquire a greater understanding of the effect of the difference between the two functional groups on the basic properties of the cluster and enlarge the scope of application using each ligand's property.

Experimental

Chemicals

All chemicals were obtained commercially and used without further purification. Hydrogen tetrachloroaurate tetrahydrate ($HAuCl_4{\cdot}4H_2O$) and chloroplatinic acid hexahydrate ($H_2PtCl_6{\cdot}6H_2O$) were from Tanaka Kikinzoku. Sodium tetrahydroborate ($NaBH_4$), tetraoctylammonium bromide ($(C_8H_{17})_4NBr$), and silica gel (spherical, 63–210 μm) were from FUJIFILM Wako Pure Chemical Co. THF, ethanol, methanol, toluene, hexane, acetonitrile, acetone, dichloromethane, and hydrogen peroxide (H_2O_2, 30 wt%) were from Kanto Chemical Co., Inc. 2-Phenylethanethiol was from Aldrich. 4-*tert*-Butylbenzenethiol and *trans*-2-[3-(4-*tert*-butylphenyl)-2-methyl-2-propenylidene]malononitrile (DCTB) were from Tokyo Chemical Industry. Co., Ltd. Cesium acetate (CH_3COOCs) was from Nacalai Tesque. Pure Milli-Q water (18.2 MΩ cm) was generated with a Merck Millipore Direct 3 UV system.

Syntheses

$Au_{24}Pt(PET)_{18}$ (1). Cluster **1** was synthesized by the method reported by Wu and co-workers[50] with a modification (Scheme S2(a)†). First, 658 mg (1.60 mmol) of $HAuCl_4{\cdot}4H_2O$, 207 mg (0.40 mmol) of $H_2PtCl_6{\cdot}6H_2O$, and 1.27 g (2.32 mmol) of $(C_8H_{17})_4NBr$ were dissolved in 60 mL of THF and the solution was stirred for 30 min at room temperature. Then, 897 μL (6.70 mmol) of 2-phenylethanethiol was added to the solution and the solution was stirred for 45 min at room temperature. The solution changed from dark to light orange. Then, 10 mL of ice-cold water was added to the reaction mixture and stirred for a further 3 min. The solution became milky white. Then, 10 mL of ice-cold water that contained 780 mg (20.0 mmol) of

$NaBH_4$ was added to the solution and the solution was stirred for 5 h at room temperature. The solution changed from light-orange to black. After the reaction, water and excess $NaBH_4$ were removed from the solution by centrifugation and THF was removed from the solution by evaporation. Excess 2-phenylethanethiol was removed with methanol, and this washing was repeated at least three times. The product was fractionated by an open column using silica gel as a stationary phase and a mixture of solvent (toluene : hexane = 5 : 3) as an eluent, and a second green fraction was collected. This fraction contained cluster **1** and $[Au_{25}(PET)_{18}]^0$. $[Au_{25}(PET)_{18}]^0$ was decomposed selectively in the mixture to obtain a high-purity cluster **1**. Crude product was dissolved in 5 mL of dichloromethane, and 5 mL of H_2O_2 was added to this solution. After stirring for 5 h, the H_2O_2 phase was removed and dichloromethane was removed by evaporation. The byproduct from the decomposition process by using H_2O_2 was removed by column chromatography using silica gel as a stationary phase and a mixture of solvent (toluene : hexane = 5 : 3) as a mobile phase. The first fraction contained the objective cluster, and ~5 mg of green cluster **1** was obtained.

$Au_{24}Pt(TBBT)_{18}$ (2). Cluster **2** was synthesized by ligand exchange of cluster **1** by 4-*tert*-butylbenzenethiol (Scheme S2(b)†). First, 5 mg (0.68 μmol) of cluster **1** was dissolved in 3.33 mL of toluene. Then, 500 μL of 4-*tert*-butylbenzenethiol was added to the solution and stirred overnight (11 h) at room temperature. The toluene was evaporated as much as possible under controlled conditions such that the temperature of the reaction mixture remained within 25 °C. Excess thiol was removed by washing with methanol. Progress of ligand exchange was monitored by ESI mass spectrometry. Because the exchange was incomplete after the first step, further ligand exchange was done in this synthesis.[35] The obtained crude mixture was dissolved in 3.33 mL of toluene and 500 μL of 4-*tert*-butylbenzenethiol, and stirred at room temperature for ~1 h. The toluene was removed, and the reaction mixture was washed with methanol until the smell of excess thiol disappeared. Crude product was purified by running a preparative TLC (silica gel 60 F_{254}, Merck) using a mixture of solvent (toluene : hexane = 3 : 7). The product purity was confirmed by HPLC and ESI-MS and an optical absorption spectrum.

Crystallization

Approximately 3 mg of the cluster **2** was dissolved in a solvent mixture of 1 mL dichloromethane and 3 drops of ethanol. The solution was placed in a smaller vial and capped loosely. The smaller vial was placed inside a bigger empty vial, which was capped tightly. Vial capping was done so that solvents evaporated slowly. Hexagonal-shaped crystals were observed after 10 days.

Characterization

Optical absorption spectra of clusters **1** and **2** were obtained in dichloromethane or trichloroethylene solutions at room temperature with a spectrometer (JASCO, V-670 or Shimadzu, UV 3600). The wavelength-dependent optical data ($I(w)$) were converted to energy-dependent data ($I(E)$) by the following equation, which conserved the integrated spectral areas: $I(E) = I(w)/|\partial E/\partial w| \propto I(w) \times w^2$.

MALDI mass spectra were collected by a spiral time-of-flight mass spectrometer (JEOL, JMSS3000) with a semiconductor laser (λ = 349 nm). DCTB was used as the MALDI matrix.[63] To minimize the cluster dissociation that was induced by laser irradiation, the cluster-to-matrix ratio was fixed at 1 : 1000.

ESI mass spectrometry was performed by using a reflectron time-of flight mass spectrometer (Bruker, micrOTOF II or Waters, Micromass Q-TOF mass spectrometer). In the measurements, a cluster solution with a concentration of 10–200 μg mL^{-1} in dichloromethane was electrosprayed at a flow rate of 180–540 μL h^{-1}.

X-ray photoelectron spectroscopy (XPS) data were collected by using an electron spectrometer (JEOL, JPS-9010MC) at a base pressure of ~2×10^{-8} Torr. X-rays from the Mg-Kα line (1253.6 eV) were used for excitation. Cluster **1** or **2** was deposited on an Ag plate, and the spectra were calibrated with the peak energies of Ag $3d_{5/2}$ (367.9 eV).[64]

A chromatogram was obtained by using a Nexera HPLC system (DGU-20A online degasser, LC-30AD pump, CTO-20AC column oven, and SPD-M30A photodiode array (PDA) detector). A YMC Meteoric Core C18 column (150 mm × 4.6 mm; i.d. 2.7 μm) was used as a core–shell reversed-phase column.[65,66] The column temperature was fixed at 25 °C to maintain reproducibility. The mobile phase with a flow rate of 1.0 mL min^{-1} was changed gradually by using a linear gradient program from acetonitrile to diethylether over 100 min. Chromatograms were monitored at 380 nm by using a PDA detector.

SCXRD data of cluster **2** were collected on a Rigaku XtaLAB Pro: XtaLAB P200 single crystal diffractometer equipped with a fine-focus sealed X-ray tube that produced multi-layer mirror-monochromated Cu Kα radiation (λ = 1.54184 Å). The crystal was kept at −173 °C during data collection. The structure was solved by a direct method using a SIR-92 structure solution program.[67] Final refinements were performed with SHELXL-2018/3 [68] by using the Olex2 platform.[69]

SWV was conducted with an electrochemical workstation (model 660B; CH Instruments) in dichloromethane with 0.1 M Bu_4NPF_6 as a supporting electrolyte that was degassed and blanketed with high-purity Ar gas. SWV was carried out with a Pt disk (0.4 mm diameter) working electrode at 100 mV s^{-1} with a pulse height and a width of 20 mV and 20 ms, respectively. Ferrocene was added as an internal reference.

Stability experiment

To investigate the stability of the clusters against decomposition in solution, an organic synthesizer (EYELA, PPS-2510) was used to control the reaction temperature precisely and reproducibly. Toluene or THF solution (10 mL, 1×10^{-5} M) of cluster **1** or cluster **2** was placed in the organic synthesizer and heated to 60 or 80 °C while stirring at 900 rpm. For the

stability test in THF, we used THF with an antioxidant (dibutylhydroxytoluene).

To investigate the stability of the clusters against laser dissociation, MALDI mass spectra were collected at a high laser fluence.

Conflicts of interest

There are no conflicts to declare.

Acknowledgements

We thank Prof. Shohei Tashiro (The University of Tokyo), Mr Kosuke Wakamatsu, and Ms Sayaka Hashimoto (Tokyo University of Science) for technical assistance. This work was supported by the Japan Society for the Promotion of Science (JSPS) KAKENHI (grant numbers JP16H04099 and 16K21402), Scientific Research on Innovative Areas "Coordination Asymmetry" (grant number 17H05385), and Scientific Research on Innovative Areas "Innovations for Light-Energy Conversion" (grant number 18H05178). Funding from the Takahashi Industrial and Economic Research Foundation, Futaba Electronics Memorial Foundation, Iwatani Naoji Foundation, and Asahi Glass Foundation is also gratefully acknowledged. D. L. acknowledges support by the Korea CCS R&D Center (KCRC) grant (NRF-2014M1A8A1074219) and NRF grants NRF-2017R1A2B3006651 and NRF-2018M3D1A1089380.

References

1 T. Tsukuda and H. Häkkinen, *Protected Metal Clusters: From Fundamentals to Applications*, Elsevier B.V., Amsterdam, The Netherlands, 2015.
2 M. Brust, M. Walker, D. Bethell, D. J. Schiffrin and R. Whyman, *J. Chem. Soc., Chem. Commun.*, 1994, 801–802.
3 R. Jin, C. Zeng, M. Zhou and Y. Chen, *Chem. Rev.*, 2016, **116**, 10346–10413.
4 H. Qian, M. Zhu, Z. Wu and R. Jin, *Acc. Chem. Res.*, 2012, **45**, 1470–1479.
5 I. Chakraborty and T. Pradeep, *Chem. Rev.*, 2017, **117**, 8208–8271.
6 Q. Yao, T. Chen, X. Yuan and J. Xie, *Acc. Chem. Res.*, 2018, **51**, 1338–1348.
7 S. Hossain, Y. Niihori, L. V. Nair, B. Kumar, W. Kurashige and Y. Negishi, *Acc. Chem. Res.*, 2018, **51**, 3114–3124.
8 K. Kwak and D. Lee, *Acc. Chem. Res.*, 2019, **52**, 12–22.
9 N. A. Sakthivel and A. Dass, *Acc. Chem. Res.*, 2018, **51**, 1774–1783.
10 R. L. Whetten, H.-C. Weissker, J. J. Pelayo, S. M. Mullins, X. López-Lozano and I. L. Garzón, *Acc. Chem. Res.*, 2019, **52**, 34–43.
11 M. Agrachev, M. Ruzzi, A. Venzo and F. Maran, *Acc. Chem. Res.*, 2019, **52**, 44–52.
12 Y. Pei, P. Wang, Z. Ma and L. Xiong, *Acc. Chem. Res.*, 2019, **52**, 23–33.
13 B. Bhattarai, Y. Zaker, A. Atnagulov, B. Yoon, U. Landman and T. P. Bigioni, *Acc. Chem. Res.*, 2018, **51**, 3104–3113.
14 C. M. Aikens, *Acc. Chem. Res.*, 2018, **51**, 3065–3073.
15 J. Yan, B. K. Teo and N. Zheng, *Acc. Chem. Res.*, 2018, **51**, 3084–3093.
16 A. Ghosh, O. F. Mohammed and O. M. Bakr, *Acc. Chem. Res.*, 2018, **51**, 3094–3103.
17 B. Nieto-Ortega and T. Bürgi, *Acc. Chem. Res.*, 2018, **51**, 2811–2819.
18 Q. Tang, G. Hu, V. Fung and D.-e. Jiang, *Acc. Chem. Res.*, 2018, **51**, 2793–2802.
19 Z. Gan, N. Xia and Z. Wu, *Acc. Chem. Res.*, 2018, **51**, 2774–2783.
20 W. Kurashige, Y. Niihori, S. Sharma and Y. Negishi, *J. Phys. Chem. Lett.*, 2014, **5**, 4134–4142.
21 Y. Song, S. Wang, J. Zhang, X. Kang, S. Chen, P. Li, H. Sheng and M. Zhu, *J. Am. Chem. Soc.*, 2014, **136**, 2963–2965.
22 Z. Lei, X.-K. Wan, S.-F. Yuan, Z.-J. Guan and Q.-M. Wang, *Acc. Chem. Res.*, 2018, **51**, 2465–2474.
23 K. Konishi, M. Iwasaki and Y. Shichibu, *Acc. Chem. Res.*, 2018, **51**, 3125–3133.
24 Q.-F. Zhang, X. Chen and L.-S. Wang, *Acc. Chem. Res.*, 2018, **51**, 2159–2168.
25 I. Ciabatti, C. Femoni, M. C. Iapalucci, S. Ruggieri and S. Zacchini, *Coord. Chem. Rev.*, 2018, **355**, 27–38.
26 E. G. Mednikov, M. C. Jewell and L. F. Dahl, *J. Am. Chem. Soc.*, 2007, **129**, 11619–11630.
27 X. Kang, H. Chong and M. Zhu, *Nanoscale*, 2018, **10**, 10758–10834.
28 T. Higaki, Q. Li, M. Zhou, S. Zhao, Y. Li, S. Li and R. Jin, *Acc. Chem. Res.*, 2018, **51**, 2764–2773.
29 M. Rambukwella, N. A. Sakthivel, J. H. Delcamp, L. Sementa, A. Fortunelli and A. Dass, *Front. Chem.*, 2018, **6**, 330.
30 C. Zeng, Y. Chen, C. Liu, K. Nobusada, N. L. Rosi and R. Jin, *Sci. Adv.*, 2015, **1**, e1500425.
31 S. Zhuang, L. Liao, M.-B. Li, C. Yao, Y. Zhao, H. Dong, J. Li, H. Deng, L. Li and Z. Wu, *Nanoscale*, 2017, **9**, 14809–14813.
32 A. Tlahuice-Flores, R. L. Whetten and M. Jose-Yacaman, *J. Phys. Chem. C*, 2013, **117**, 20867–20875.
33 A. Tlahuice-Flores, *Phys. Chem. Chem. Phys.*, 2016, **18**, 27738–27744.
34 J. Jung, S. Kang and Y.-K. Han, *Nanoscale*, 2012, **4**, 4206–4210.
35 M. Rambukwella, S. Burrage, M. Neubrander, O. Baseggio, E. Aprà, M. Stener, A. Fortunelli and A. Dass, *J. Phys. Chem. Lett.*, 2017, **8**, 1530–1537.
36 R. R. Nasaruddin, T. Chen, J. Li, N. Goswami, J. Zhang, N. Yan and J. Xie, *ChemCatChem*, 2018, **10**, 395–402.
37 R. R. Nasaruddin, T. Chen, N. Yan and J. Xie, *Coord. Chem. Rev.*, 2018, **368**, 60–79.

38 D. M. Chevrier, L. Raich, C. Rovira, A. Das, Z. Luo, Q. Yao, A. Chatt, J. Xie, R. Jin, J. Akola and P. Zhang, *J. Am. Chem. Soc.*, 2018, **140**, 15430–15436.
39 F. Bertorelle, I. Russier-Antoine, C. Comby-Zerbino, F. Chirot, P. Dugourd, P.-F. Brevet and R. Antoine, *ACS Omega*, 2018, **3**, 15635–15642.
40 G. Li, H. Abroshan, C. Liu, S. Zhuo, Z. Li, Y. Xie, H. J. Kim, N. L. Rosi and R. Jin, *ACS Nano*, 2016, **10**, 7998–8005.
41 T. Omoda, S. Takano and T. Tsukuda, *Chem. Lett.*, 2019, **48**, 885–887.
42 Z. Wu and R. Jin, *Nano Lett.*, 2010, **10**, 2568–2573.
43 C. Zeng, C. Liu, Y. Pei and R. Jin, *ACS Nano*, 2013, **7**, 6138–6145.
44 C. Zeng, Y. Chen, A. Das and R. Jin, *J. Phys. Chem. Lett.*, 2015, **6**, 2976–2986.
45 S. K. Eswaramoorthy, N. A. Sakthivel and A. Dass, *J. Phys. Chem. C*, 2019, **123**, 9634–9639.
46 C. Zeng, T. Li, A. Das, N. L. Rosi and R. Jin, *J. Am. Chem. Soc.*, 2013, **135**, 10011–10013.
47 Y. Negishi, W. Kurashige, Y. Niihori, T. Iwasa and K. Nobusada, *Phys. Chem. Chem. Phys.*, 2010, **12**, 6219–6225.
48 H. Qian, D.-e. Jiang, G. Li, C. Gayathri, A. Das, R. R. Gil and R. Jin, *J. Am. Chem. Soc.*, 2012, **134**, 16159–16162.
49 K. Kwak, W. Choi, Q. Tang, M. Kim, Y. Lee, D.-e. Jiang and D. Lee, *Nat. Commun.*, 2017, **8**, 14723.
50 S. Tian, L. Liao, J. Yuan, C. Yao, J. Chen, J. Yang and Z. Wu, *Chem. Commun.*, 2016, **52**, 9873–9876.
51 F. Alkan, P. Pandeya and C. M. Aikens, *J. Phys. Chem. C*, 2019, **123**, 9516–9527.
52 F. G. Bordwell, *Acc. Chem. Res.*, 1988, **21**, 456–463.
53 M. Zhu, H. Qian and R. Jin, *J. Am. Chem. Soc.*, 2009, **131**, 7220–7221.
54 C. Zeng, C. Liu, Y. Chen, N. L. Rosi and R. Jin, *J. Am. Chem. Soc.*, 2014, **136**, 11922–11925.
55 P. Wang, X. Sun, X. Liu, L. Xiong, Z. Ma, Y. Wang and Y. Pei, *Nanoscale*, 2018, **10**, 10357–10364.
56 K. Kwak, Q. Tang, M. Kim, D.-e. Jiang and D. Lee, *J. Am. Chem. Soc.*, 2015, **137**, 10833–10840.
57 R. Guo and R. W. Murray, *J. Am. Chem. Soc.*, 2005, **127**, 12140–12143.
58 M. Zhou, H. Qian, M. Y. Sfeir, K. Nobusada and R. Jin, *Nanoscale*, 2016, **8**, 7163–7171.
59 W. Kurashige, M. Yamaguchi, K. Nobusada and Y. Negishi, *J. Phys. Chem. Lett.*, 2012, **3**, 2649–2652.
60 W. Kurashige, R. Hayashi, K. Wakamatsu, Y. Kataoka, S. Hossain, A. Iwase, A. Kudo, S. Yamazoe and Y. Negishi, *ACS Appl. Energy Mater.*, 2019, **2**, 4175–4187.
61 G. Li and R. Jin, *Acc. Chem. Res.*, 2013, **46**, 1749–1758.
62 X. Kang and M. Zhu, *Chem. Soc. Rev.*, 2019, **48**, 2422–2457.
63 A. Dass, A. Stevenson, G. R. Dubay, J. B. Tracy and R. W. Murray, *J. Am. Chem. Soc.*, 2008, **130**, 5940–5946.
64 J. C. Fuggle, E. Källne, L. M. Watson and D. J. Fabian, *Phys. Rev. B: Solid State*, 1977, **16**, 750–761.
65 Y. Niihori, Y. Koyama, S. Watanabe, S. Hashimoto, S. Hossain, L. V. Nair, B. Kumar, W. Kurashige and Y. Negishi, *J. Phys. Chem. Lett.*, 2018, **9**, 4930–4934.
66 Y. Niihori, S. Hashimoto, Y. Koyama, S. Hossain, W. Kurashige and Y. Negishi, *J. Phys. Chem. C*, 2019, **123**, 13324–13329.
67 A. Altomare, G. Cascarano, C. Giacovazzo, A. Guagliardi, M. C. Burla, G. Polidori and M. Camalli, *J. Appl. Crystallogr.*, 1994, **27**, 435–436.
68 G. M. Sheldrick, *Acta Crystallogr., Sect. C: Struct. Chem.*, 2015, **71**, 3–8.
69 O. V. Dolomanov, L. J. Bourhis, R. J. Gildea, J. A. K. Howard and H. Puschmann, *J. Appl. Crystallogr.*, 2009, **42**, 339–341.